RSC Advances

PAPER

View Article Online
View Journal | View Issue

Cite this: *RSC Adv.*, 2025, **15**, 27403

Ternary MgZ_2N_4 (Z = Ge, Si) and Janus $MgGeSiN_4$ monolayers: high stability with distinctive electronic and magnetic properties

Warda Elaggoune, *[a] Yusuf Zuntu Abdullahi,[bc] Sohail Ahmad[d] and Lim Thong Leng[e]

Received 4th June 2025
Accepted 25th July 2025

DOI: 10.1039/d5ra03942h

rsc.li/rsc-advances

The recent synthesis of two-dimensional (2D) $MoSi_2N_4$ and WSi_2N_4 crystals has given rise to a new class of 2D materials with distinctive properties and significant potential for advanced technologies. The transition metal (TM) elements can potentially be substituted with other elements from the periodic table, enabling the introduction of new members into this emerging 2D family. Building on this framework, we propose a new family of light-element-based 2D ternary compounds of MgZ_2N_4 (Z = Si, Ge) and their Janus derivative $MgGeSiN_4$ using first-principles density functional theory (DFT) calculations. All three monolayers are found to be dynamically, thermally, and mechanically stable. $MgGe_2N_4$ exhibits a metallic antiferromagnetic (AFM) ground state within the PBE functional, while more accurate HSE-level calculations reveal a weak ferrimagnetic (FiM) configuration. Conversely, $MgSi_2N_4$ is a robust half-metallic ferromagnet with 100% spin polarization and a sizable magnetic moment of 5.62μ_B per unit cell. Janus $MgGeSiN_4$ shows FiM metallic behavior, driven by structural asymmetry. All systems favor an in-plane easy axis magnetization, and our analysis shows that their magnetic behavior follows a unique low-temperature Berezinskii–Kosterlitz–Thouless (BKT) transition, characteristic of the 2D XY-like model. The estimated BKT transition temperatures for $MgGe_2N_4$, $MgSi_2N_4$, and $MgGeSiN_4$ are approximately 19 K, 4 K, and 16 K, respectively. This study presents the first report of intrinsic FM, AFM, and FiM in this monolayer family, highlighting their potential for advanced low-temperature magnetic device applications.

1 Introduction

The rapid expansion of research on 2D materials continues to push the boundaries of low-dimensional magnetism, particularly in the pursuit of spin-based phenomena for next-generation spintronic devices. Although the discovery of graphene initiated an era of intense exploration of atomically thin systems,[1] the more recent isolation of intrinsically magnetic 2D materials has opened a new chapter in the study of magnetism at the nanoscale.[2] This breakthrough has led to the synthesis and theoretical prediction of numerous 2D magnetic materials, such as CrI_3,[3] $Cr_2Ge_2Te_6$,[4] and Fe_3GeTe_2,[5] demonstrating that long-range magnetic order can indeed persist in the 2D limit due to spin–orbit coupling–induced anisotropy and symmetry breaking.

Following this trend, a novel family of layered 2D materials with the general formula MA_2Z_4 has emerged, offering tunable structures and promising functionalities for a wide range of advanced applications. Here, M denotes the transition metals from groups IVB, VB, or VIB; A is Si or Ge; and Z represents N, P, or As. In 2020, Hong *et al.*[6] successfully synthesized high-quality septuple-layer $MoSi_2N_4$ and WSi_2N_4 monolayers *via* chemical vapor deposition (CVD), initiating this intriguing materials class. These monolayers exhibit excellent ambient stability and have sparked extensive theoretical investigations into other MA_2Z_4 compounds, including twelve WSi_2N_4 polymorphs characterized by various α_i and β_i phases.[7]

Despite their outstanding properties, most MA_2Z_4 monolayers are intrinsically non-magnetic, limiting their direct applicability in spintronics. To overcome this, doping strategies, particularly substitutional or interstitial doping have proven effective in inducing and tuning magnetism without significantly disrupting structural stability.[8] Substitutional doping, in particular, enables the precise replacement of M, A, or Z atoms with magnetic transition metals or other elements, often resulting in spin-polarized impurity states and long-range magnetic ordering.

As a results, several MA_2Z_4-based systems have been proposed for spin-based applications. For instance, WSi_2P_4 has been suggested for spin-valley polarization, $TaSi_2N_4$ for Ising superconductivity, and $SrGa_2Se_4$ as a topological insulator.[9]

[a]*Laboratoire de Physique des Matériaux (L2PM), Faculté des Mathématiques, de l'informatique et des Sciences de la Matière, Université 8 Mai 1945, BP 401, Guelma, Algeria. E-mail: elaggoune.warda@univ-guelma.dz*

[b]*Department of Physics, Aydin Adnan Menderes University, Aydin 09010, Turkey*

[c]*Department of Physics, Faculty of Science, Kaduna State University, P.M.B. 2339, Kaduna State, Nigeria*

[d]*Department of Physics, College of Science, King Khalid University, P O Box 9004, Abha, Saudi Arabia*

[e]*Faculty of Engineering and Technology, Multimedia University, Jalan Ayer Keroh Lama, 75450 Melaka, Malaysia*

Spin-valley coupling phenomena have also been explored in $MoSi_2N_4$, WSi_2N_4, and $MoSi_2As_4$.[9] Notably, strain-induced ferromagnetism has been reported in VSi_2P_4 and VSi_2N_4,[10] and several dynamically stable magnetic monolayers have been identified, including VSi_2N_4, $NbSi_2N_4$, $NbGe_2N_4$, $TaGe_2N_4$, and YSi_2N_4.[11,12] Most of these exhibit semiconducting ferromagnetism, except for YSi_2N_4, which is a metallic ferromagnet.[12] Additionally, $ScSi_2N_4$ has been predicted as a half-metal with in-plane magnetic anisotropy,[13] while $HfCr_2N_4$ shows strain-tunable magnetism and an antiferromagnetic ground state.[14]

Atomic composition plays a decisive role in determining the stability and electronic behavior of MA_2Z_4 structures. Wang *et al.*[7] systematically investigated 54 MA_2Z_4 compounds. Here, A = Mg, Ca, Sr and M = Zn, Cd, Hg, containing 32–34 valence electrons, and identified 36 energetically favorable semiconducting monolayers. Motivated by these advances, we propose a new subclass of ternary magnetic MA_2Z_4 monolayers with the chemical formula MgX_2N_4 (X = Si, Ge), containing 30 valence electrons, based on DFT calculations. The substitution of transition metals with magnesium in MA_2Z_4 monolayers offers a compelling strategy to design novel 2D materials with unconventional properties. Mg, being earth-abundant, non-toxic, and electronically closed-shell, enables a shift away from traditional d-orbital-driven magnetism toward a p-orbital-mediated regime, unlocking unexpected magnetic behaviors.[15] This approach not only expands the compositional landscape of MA_2Z_4 monolayers but also introduces lightweight, sustainable alternatives with tunable electronic and magnetic characteristics. By leveraging the distinctive septuple-layer architecture and high chemical flexibility of the MA_2Z_4 framework, we systematically investigate the structural integrity, electronic features, and magnetic ordering of this new class of Mg-based compounds.

In addition, we investigated the Janus $MgSiGeN_4$ monolayer. Janus materials have shown significant promise in spintronics applications. For example, Janus $VSiGeP_2As_2$ exhibits robust ferromagnetism and strong in-plane magnetic anisotropy,[16] while Janus $MSiGeN_4$ (M = Zr, Hf) undergoes strain-induced transitions from semiconducting to metallic states.[17] Furthermore, Janus $VSiGeN_4$ and $VSiSnN_4$ demonstrate narrow-bandgap semiconducting behavior with weak easy-plane magnetic anisotropy, distinguishing them from their VSi_2N_4 counterparts.[18]

Our results reveal that $MgGe_2N_4$ is a ferrimagnetic metal with weak magnetism, $MgSi_2N_4$ is a half-metallic ferromagnet with full spin polarization (insulating in spin-up and metallic in spin-down channels), and Janus $MgSiGeN_4$ is also a ferrimagnetic metal. All three monolayers prefer an in-plane easy axis for the magnetic anisotropy, with BKT transition temperatures estimated at 19 K, 4 K, and 16 K for $MgGe_2N_4$, $MgSi_2N_4$, and $MgSiGeN_4$, respectively. These distinctive electronic and magnetic properties position them as promising candidates for future magnetic nanodevice applications.

2 Computational details

We carried out DFT calculations with the aid of the Vienna *Ab initio* Simulation Package (VASP)[19–22] to investigate the structural, electronic, and magnetic properties of MgX_2N_4 (X = Ge, Si) and their Janus derivative $MgGeSiN_4$ monolayers. The electron exchange–correlation interactions for spin-polarized case were treated within the generalized gradient approximation (GGA) using the Perdew–Burke–Ernzerhof (PBE) functional.[23] The interaction between core and valence electrons was described by the projector augmented wave (PAW) method,[24] with the valence electron configurations considered for Mg, Si/Ge, and N elements.

A plane-wave energy cutoff of 500 eV was used for the expansion of wave functions. A vacuum space of 18 Å along the out-of-plane (z) direction was introduced to eliminate interlayer interactions due to periodic boundary conditions. Brillouin zone integrations were performed using an optimized Monkhorst–Pack k-point mesh, ensuring total energy convergence within 0.001 eV per atom.

The structural relaxations were carried out by simultaneously optimizing both the lattice parameters and atomic positions until the Hellmann–Feynman forces on each atom were reduced below 0.01 eV $Å^{-1}$, the total energy difference between consecutive ionic steps was less than 1×10^{-6} eV, and the maximum pressure within the simulated cells was minimized to under 0.1 kbar.

To obtain a more accurate estimation of the electronic band structure and bandgap, hybrid functional calculations were performed using the Heyd–Scuseria–Ernzerhof (HSE06) formalism.[25] To account for dispersion interactions, Grimme's DFT-D3 van der Waals correction was included during geometry optimizations.[26]

To gain insight into the charge redistribution and bonding nature, Bader charge analysis and the electron localization function (ELF) were evaluated, facilitating a detailed understanding of interatomic charge transfer and bonding characteristics.[27] The phonon dispersion spectra were computed using the PHONOPY[28] code interfaced with VASP to assess the dynamical stability of the monolayers.

Furthermore, *ab initio* molecular dynamics (AIMD) simulations were performed on a $2 \times 2 \times 1$ supercell using the canonical (NVT) ensemble regulated by the Nosé thermostat,[8] with a time step of 1 fs over a total simulation time of 5 ps at 300 K, to evaluate the thermal stability of the proposed structures.

Finally, the VASPKIT toolkit[29] was employed for post-processing and extracting elastic constants and other mechanical properties from the calculated data.

3 Results and discussions

3.1 Geometries and phase stability

The crystal structures of the proposed $MgGe_2N_4$, $MgSi_2N_4$, and Janus $MgGeSiN_4$ monolayers were designed by adapting the geometric framework of the experimentally synthesized 1H-phase of $MoSi_2N_4$ and WSi_2N_4 monolayers.[6] These materials adopt a layered configuration characterized by a hexagonal lattice and belong to the $P6m2$ (No. 187) space group, displaying D_{3h} symmetry. The optimized monolayers consist of a seven-atom-thick slab with the atomic stacking sequence N–Z–N–Mg–N–Z–N (Z = Si or Ge), forming robust layered networks.

Representative top and side views of $MgSi_2N_4$ unit cell are shown in Fig. 1(a) and (c). The Janus derivative, $MgGeSiN_4$, is constructed by replacing one Ge layer in $MgGe_2N_4$ with a Si layer. This modification breaks the out-of-plane mirror symmetry associated with the Mg atomic plane, reducing the overall point group symmetry from D_{3h} to C_{3v}, while preserving in-plane symmetry. The resulting Janus configuration shows the opposite atomic orientation, as reflected in the N–Ge–N–Mg–N–Si–N stacking sequence (see Fig. 1(b) and (d)).

To identify the magnetic ground state, we performed spin-polarized supercell calculations considering one ferromagnetic (FM) and two antiferromagnetic (AFM) configurations, denoted AFM_1 and AFM_2. In the AFM_1 configuration, the magnetic moments on the neighboring atoms are aligned antiparallel orientation within the unit cell. Conversely, in the FM configuration, all magnetic moments are aligned in the same direction. In all cases, spin orientations are set perpendicular to the atomic plane (out-of-plane), as indicated by the red (up) and blue (down) arrows. The top views of the most energetically favorable (2×2) supercell structures are shown in Fig. 1e–g, while additional considered configurations that are found to be less stable are presented in Fig. S1. The magnetic ground state is determined by comparing the total energy differences between the AFM and FM configurations (Δ_{AFM-FM}), as reported later in Table 2. Our calculations reveal that the $MgGe_2N_4$ and the Janus $MgGeSiN_4$ monolayers stabilize in the AFM_1 configuration, indicated by negative Δ_{AFM-FM} values. In contrast, a positive energy difference for $MgSi_2N_4$ suggests FM ground state, similar with previous findings for Si-based VSi_2N_4 monolayers and their Janus derivatives.[11,12,16]

Table 1 summarizes the optimized lattice parameters, bond lengths (l_{in} and l_{out}), bond angles (θ), and overall thickness (h) of

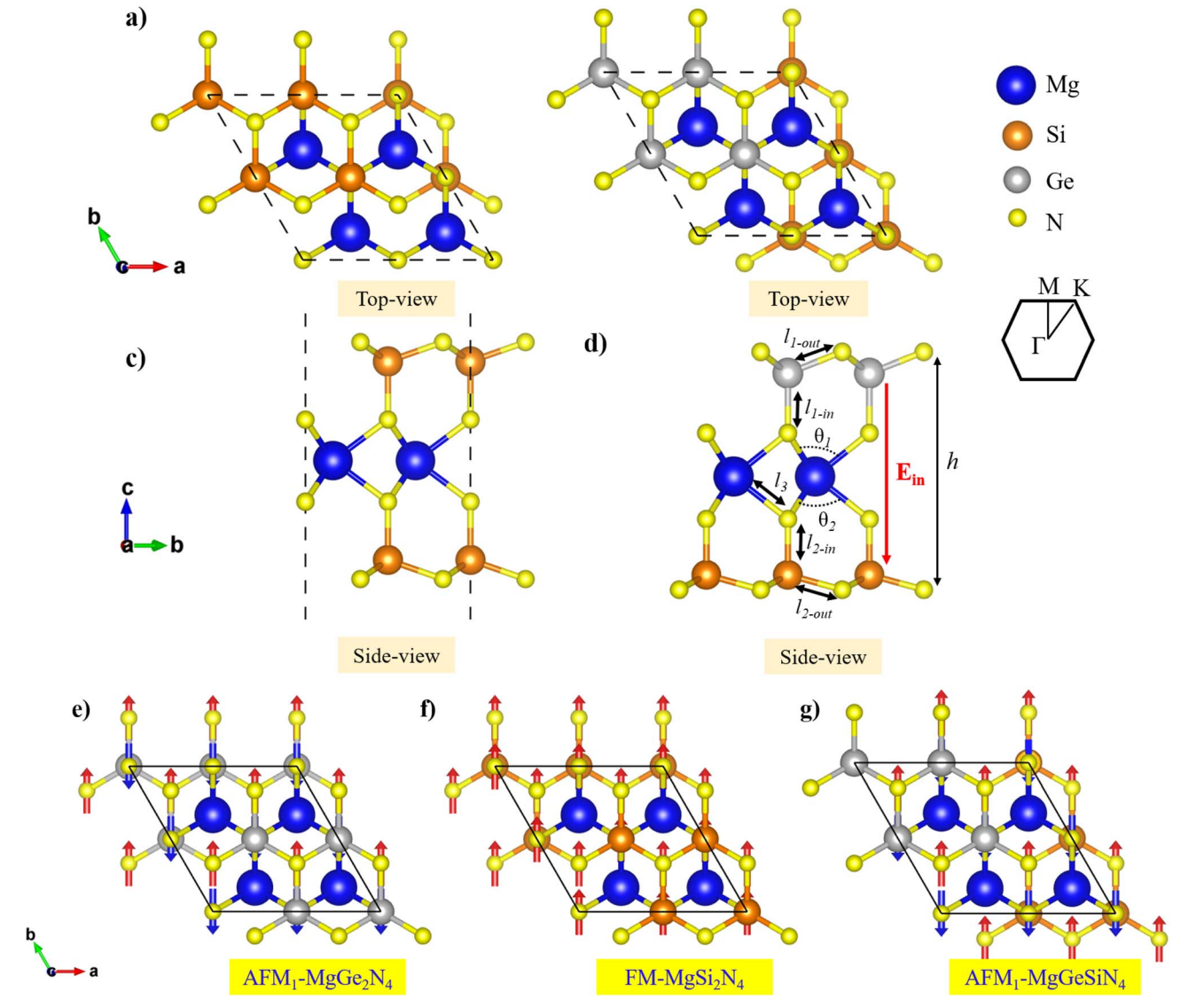

Fig. 1 (a and b) Top and (c and d) side views of the crystal structures of pristine MgZ_2N_4 (Z = Ge, Si) and Janus $MgGeSiN_4$ monolayers, with bond lengths and bond angles indicated for the top and bottom layers. (e–g) Top views of the most energetically favorable magnetic configurations. He high-symmetry path within the first Brillouin zone is also shown.

Table 1 The optimized structural parameters of $MgGe_2N_4$, $MgSi_2N_4$, and Janus $MgGeSiN_4$: lattice constant $a = b$, inter Si–N bond length $l_{1\text{-in}}$, outer Si–N bond length $l_{1\text{-out}}$, inter Ge–N bond length $l_{2\text{-in}}$, outer Ge–N bond length $l_{2\text{-out}}$, Mg–N bond length l_3, layer thickness h, bond angles for the top (bottom) layer θ_1 (θ_2)), cohesive energy E_{coh}, formation energy E_{form}, and elastic constants C_{11} and C_{11} of MgZ_2N_4 (Z = Ge, Si) and Janus $MgGeSiN_4$ monolayers

Material	$a = b$ (Å)	$l_{1\text{-in}}$ (Å)	$l_{1\text{-out}}$ (Å)	$l_{2\text{-in}}$ (Å)	$l_{2\text{-out}}$ (Å)	l_3 (Å)	h (Å)	θ_1 (eV)	θ_2 (eV)	E_{coh} (eV)	E_{form} (eV)	C_{11} (N m^{-1})	C_{12} (N m^{-1})
$MgGe_2N_4$	3.09	—	—	1.89	1.89	2.22	8.28	87.85	87.85	3.93	−2.14	235.29	146.75
$MgSi_2N_4$	2.91	1.77	1.75	—	—	2.17	7.88	83.86	83.85	4.91	−2.90	366.970	111.19
$MgGeSiN_4$	2.99	1.90	1.85	1.77	1.79	2.19	8.12	84.98	86.06	4.39	−2.50	206.54	176.56
WGe_2N_4 (ref. 30)	3.04	—	—	1.89	1.86	2.10	7.02	—	—	5.44	—	449.85	140.96
WSi_2N_4 (ref. 30)	2.91	1.74	1.75	—	—	2.10	7.02	—	—	6.44	—	565.62	158.12
$WGeSiN_4$ (ref. 30)	2.97	1.75	1.78	1.89	1.84	2.11	7.27	—	—	5.92	—	504.53	148.17
$TiSi_2N_4$ (ref. 37)	2.92	2.06	—	1.75	1.76	—	—	70.63	107.07	—	—	725.52	232.29
$ZrSiGeN_4$ (ref. 17)	3.11	—	—	—	—	—	—	—	—	—	—	403.92	110.58
$HfSiGeN_4$ (ref. 17)	3.10	—	—	—	—	—	—	—	—	—	—	465.93	135.19
$RuSi_2N_4$ (ref. 31)	2.95	2.07	—	—	—	—	6.83	—	—	5.77	—	—	—
$OsSi_2N_4$ (ref. 31)	2.97	2.08	—	—	—	—	6.84	—	—	5.73	—	—	—

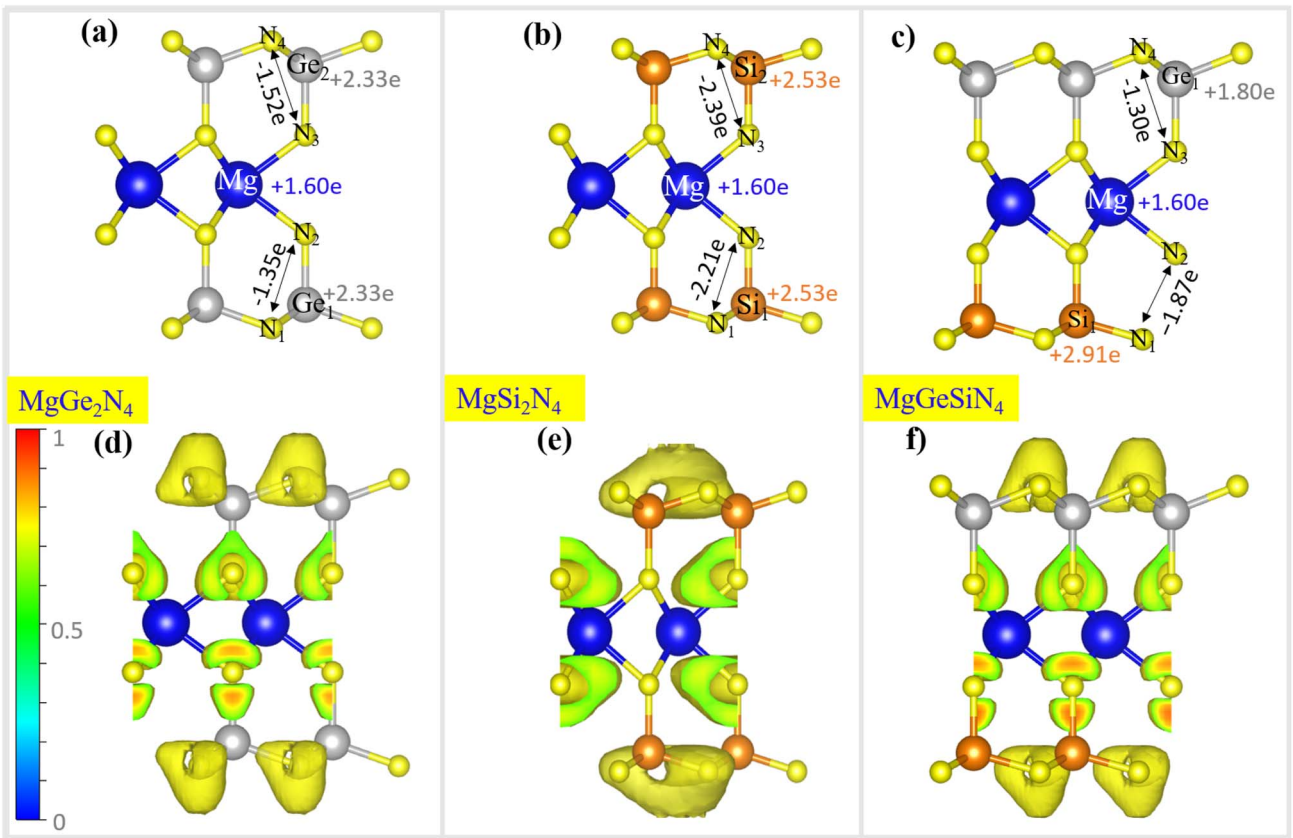

Fig. 2 (a–c) Charge transfer distributions obtained from Bader charge analysis, and (d–f) 3D electron localization function (ELF) isosurfaces for MgZ_2N_4 (Z = Ge, Si) and Janus $MgGeSiN_4$ monolayers.

the three systems. Notably, the in-plane lattice constant of Janus $MgGeSiN_4$ lies between those of its symmetric counterparts and increases with the atomic number of the Z element, consistent with previously reported trends in Janus 2D materials (see Table 1).[30] In particular, similar variations are also observed in other structural parameters, such as Ge–N, Si–N, and Mg–N bond lengths, bond angles, and the thickness, confirming that the Janus configuration induces an intrinsic geometric asymmetry throughout the lattice. This structural perturbation is expected to influence the electronic properties of the material. These findings align well with those of previous investigations (Table 1).

To gain a deeper understanding of the bonding nature in $MgSi_2N_4$, $MgGe_2N_4$, and Janus $MgGeSiN_4$ monolayers, we first

examine the Bader charge analysis, which quantifies charge redistribution among the constituent atoms (see Fig. 2a–c). In all three systems, the Mg atoms consistently act as electron donors, transferring approximately $+1.60e^-$ to their surrounding N atoms. In $MgGe_2N_4$, the Ge atoms donate a substantial amount of charge ($+2.33e^-$), while each N atom receives approximately -1.35 to $-1.52e^-$, indicating a strong polar interaction and significant electron accumulation around N. A similar, though slightly enhanced, trend is observed in $MgSi_2N_4$, where the Si atoms contribute $+2.53e^-$, and the N atoms accumulate about -2.21 to $-2.39e^-$, suggesting stronger charge transfer. In the Janus $MgGeSiN_4$ structure, the asymmetric distribution becomes apparent: Si atoms on the bottom surface donate $+2.91e^-$, whereas Ge atoms on the top contribute only $+1.80e^-$. N atoms near the Si side gain more charge ($-1.87e^-$) compared to those closer to Ge ($-1.30e^-$), establishing a built-in dipole moment across the vertical axis of the monolayer. These results are consistent with those observed in $WGeSiN_4$ Janus.[30]

The Electron Localization Function (ELF) plots further support these charge transfer trends by revealing the spatial distribution of electrons in the bonding regions (see Fig. 2d–f). In $MgGe_2N_4$, the ELF contour maps show pronounced electron localization between the Ge and N atoms, with localization values ranging from 0.80 to 0.85. This clearly points to strong directional covalent bonding, enabled by the higher electronegativity of Ge. For $MgSi_2N_4$, the ELF intensity between Si and N is markedly reduced, dropping to ~0.65–0.75, with broader and more diffuse charge clouds, reflecting a weaker polar covalent character due to tighter Si–N bond distances. The Janus $MgGeSiN_4$ monolayer exhibits a clear ELF asymmetry: the Si–N side shows strong ELF ~0.80, while the Ge–N side shows diluted and less concentrated contours (~0.70).

The cohesive energy (E_{coh}) is used to assess the energetic feasibility of the proposed structures and is defined as the amount of energy required to separate a condensed material into its constituent isolated atoms. The E_{coh} of each structure is calculated using the following expression:

$$E_{coh} = \frac{E_{Mg} + 2E_Z + 4E_N - E_T}{7} \quad (1)$$

where E_T is the total energy of the fully relaxed monolayers $MgGe_2N_4$, $MgSi_2N_4$, and Janus $MgGeSiN_4$, and E_{Mg}, E_Z (Z = Ge or Si), and E_N represent the total energies of isolated Mg, Ge (or Si), and N atoms, respectively. The numerical coefficients reflect the number of each atom type in the unit cell.

All computed E_{coh} values, summarized in Table 1, are positive and relatively large, indicating strong cohesive interactions and confirming the energetic stability of the monolayers, suggesting their potential feasibility for experimental synthesis. Additionally, the E_{coh} values are found to depend on the atomic radius of element Z: a larger atomic radius typically results in a slightly lower cohesive energy, due to weaker bonding interactions. Notably, the cohesive energy of Janus $MgGeSiN_4$ lies nearly at the midpoint between those of $MgGe_2N_4$ and $MgSi_2N_4$, consistent with its geometrical parameters.

In comparison with previously reported systems such as WSi_2N_4, WGe_2N_4, $RuSi_2N_4$, $OsSi_2N_4$ and the Janus $WSiGeN_4$ monolayers (see Table 1), as well as other well-studied 1T-phase materials like 1T-$RuSi_2N_4$ (5.87 eV per atom) and 1T-$OsSi_2N_4$ (5.87 eV per atom),[31] the E_{coh} of our proposed 1H-based MgZ_2N_4 (Z = Ge, Si) and Janus $MgGeSiN_4$ monolayers are slightly lower. However, they remain significantly positive and substantial, reflecting strong interatomic interactions and structural cohesion. The relatively reduced E_{coh} values can be attributed primarily to two factors: (i) the lighter atomic masses and lower electronegativity of the Mg, Ge, and Si constituents, which naturally lead to comparatively weaker bonding interactions than those observed in heavy transition-metal-based analogs; and (ii) the absence of partially filled d-orbitals in Mg, which diminishes the possibility of strong d-orbital hybridization, a key contributor to the enhanced cohesive strength in Ru-, Os-, and W-containing systems.

The formation energy per atom (E_{form}) is further employed to evaluate the thermodynamic stability and acts as an indicator to quantify the energy needed to construct a given structure from its constituent atoms. The E_{form} of each structure is calculated using the following expression:

$$E_{for} = (E_T - \mu_{Mg} - 2\mu_Z - 4\mu_N)/7 \quad (2)$$

Here, E_T is the total energy of the fully relaxed monolayers $MgGe_2N_4$, $MgSi_2N_4$, and Janus $MgGeSiN_4$, μ_{Mg}, μ_Z, and μ_N represent the chemical potentials of the Mg, Z (Z = Ge and Si) and N atoms, defined as the total energy per atom of each element in its most stable bulk form. Mg crystallizes in a hexagonal structure with $P6_3/mmc$ space group, Ge and Si assume cubic structures with $Fd\bar{3}m$ space group, and N is cubic alpha N_2 structured and crystallizes in the cubic $P2_13$ space group. The calculated results are summarized in Table 1.

The negative values of E_{form} indicate that the MgZ_2N_4 monolayers and their Janus counterpart, $MgGeSiN_4$, are thermodynamically stable and exothermic in nature, suggesting their potential synthesizability under suitable experimental conditions. Furthermore, consistent with the trends observed in geometrical parameters and E_{coh}, the E_{form} of Janus $MgGeSiN_4$ lies nearly midway between those of $MgGe_2N_4$ and $MgSi_2N_4$, reflecting its compositional average. The calculated values are also comparable to or more favorable than those reported for W-doped $MoSi_2N_4$ (-2.18 eV) and W-doped WSi_2N_4 (-2.31 eV), and are significantly lower (*i.e.*, more stable) than those of Hf- and Ta-doped $MoSi_2N_4$ (-0.06 eV and -0.91 eV, respectively).[32]

The mechanical stability of the 2D $MgGe_2N_4$, $MgSi_2N_4$ and Janus $MgGeSiN_4$ monolayers is systematically evaluated using the Born–Huang stability criteria.[33] Due to their hexagonal symmetry, only two independent elastic constants. Namely C_{11} and C_{12} are required to assess the in-plane mechanical response. As presented in Table 1, all the calculated elastic constants satisfy the mechanical stability conditions, namely $C_{11} > 0$ and $C_{11} > |C_{12}|$. These results confirm that these monolayers are mechanically stable under small elastic deformations, further supporting their potential for experimental synthesis and integration into strain-engineered nanodevices.

The calculated values of the elastic constants reveal insightful mechanical trends in our monolayers. Specifically, the C_{11} values are generally lower than those of several comparable 2D materials reported in Table 1. In contrast, the C_{12} values are significantly higher than those reported for many of the benchmark materials in the same references. The elastic constant C_{11} primarily characterizes the material's resistance to uniaxial compression along the in-plane x-direction, whereas C_{12} is associated with the material's lateral response under in-plane stress.[34–36] These results, particularly Janus $MgGeSiN_4$, which exhibits the smallest C_{11} and the highest C_{12}, indicate a mechanically anisotropic nature, characterized by enhanced lateral rigidity coupled with axial softness. Such a unique mechanical profile is highly advantageous for strain-engineered applications and the development of flexible electronic devices.

The mechanical properties, specifically, Young's modulus (Y) and Poisson's ratio (ν) are derived from the elastic constants using the following relations:

$$Y = \frac{{C_{11}}^2 - {C_{12}}^2}{C_{11}}, \quad \nu = \frac{C_{12}}{C_{11}}. \tag{3}$$

The calculated Y and ν for pristine MgZ_2N_4 (Z = Ge, Si) and Janus $MgGeSiN_4$ monolayers are presented in the histogram shown in Fig. S2, alongside other related compounds from the same material family for comparative visualization.

Specifically, $MgGe_2N_4$ exhibits a Y of 143.76 N m^{-1} and a ν of 0.62, while $MgSi_2N_4$ shows a significantly higher Y of 333.28 N m^{-1} and a lower ν of 0.30. In contrast, the Janus $MgGeSiN_4$ monolayer displays a much lower Y of 55.61 N m^{-1} and a relatively high ν of 0.86. These monolayers demonstrate isotropic mechanical behavior in both Y and ν, consistent with their underlying hexagonal symmetry. Interestingly, despite the broken mirror symmetry in the Janus $MgGeSiN_4$ monolayer, it still retains isotropic mechanical properties, indicating structural robustness. Compared to other monolayers, electronegativity is found to play a critical role in the influence of the Y value. Elements with higher electronegativity values—such as W (2.36), Hf (1.88), and Zr (1.33)—result in stiffer bonding networks in the structure and consequently higher Y values, compared to Mg (1.31), which forms weaker and more ionic bonds. Among the studied monolayers, $MgSi_2N_4$ exhibits the highest in-plane stiffness, as indicated by its large C_{11} value. Similar behavior has been reported in other MA_2Z_4-type 2D materials incorporating Si or Ge.[17,30] The lower Y value observed for Janus $MgGeSiN_4$ is mainly attributed to the larger atomic radius of Mg and the absence of d-orbital participation, as discussed previously, which collectively reduce resistance to axial deformation compared to transition-metal-based analogs.

Electronegativity also significantly impacts Poisson's ratio. Among the studied compounds, $MgGeSiN_4$ exhibits a relatively high Poisson's ratio, which is a direct consequence of its soft bonding network. This allows substantial lateral deformation under axial stress, even though the material exhibits limited axial stiffness.

To validate the dynamical stability of the studied monolayers, we calculated their phonon band dispersions along the high-symmetry directions using density functional perturbation theory (DFPT),[28] as shown in Fig. 3 (a–c). As is evident, the phonon spectra of pristine $MgGe_2N_4$ and $MgSi_2N_4$ and their $MgGeSiN_4$ Janus counterpart exhibit no imaginary frequencies

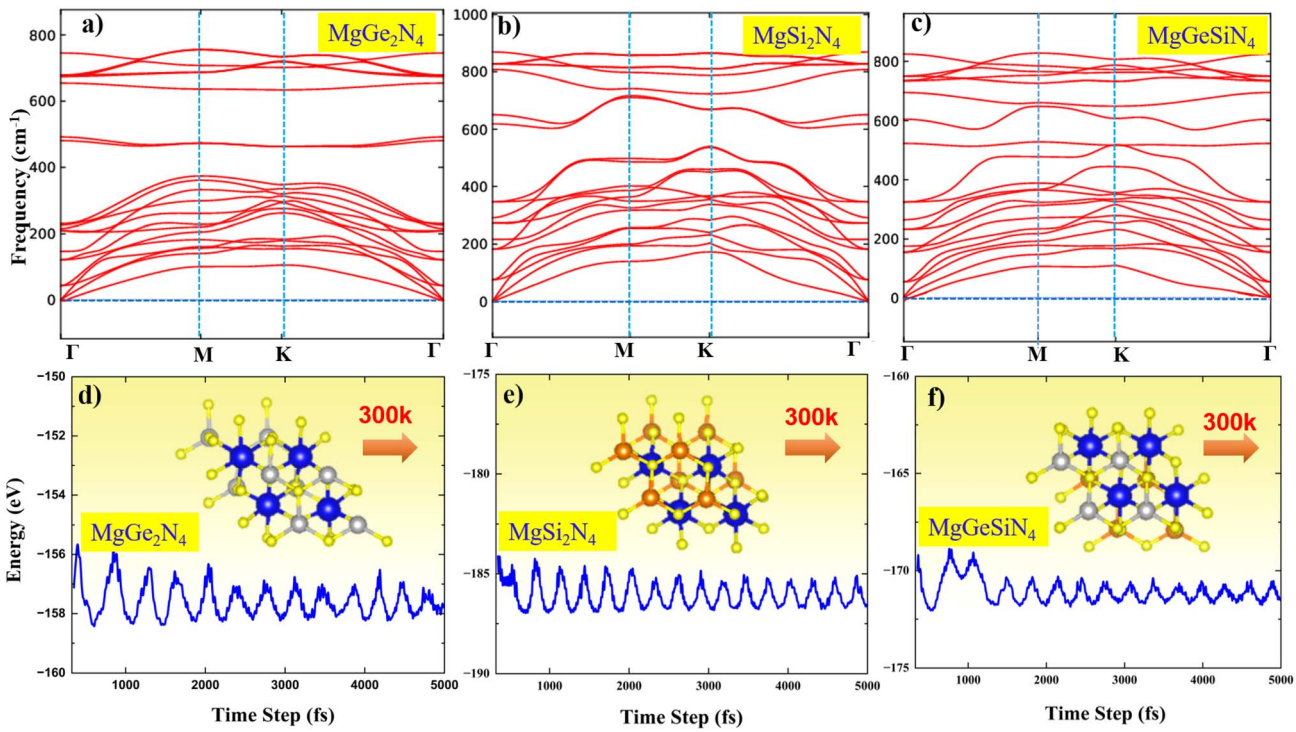

Fig. 3 (a–c) Phonon dispersion curves and (d–f) energy evolution during AIMD simulations for 5 ps at 300 K for MgZ_2N_4 (Z = Ge, Si) and Janus $MgGeSiN_4$ monolayers. The insets include top view snapshots of the final geometries for each structure.

throughout the entire Brillouin zone, confirming their dynamical stability and indicating that these compounds may be experimentally realizable. All three systems exhibit three acoustic and 18 optical phonon branches, consistent with the seven atoms per unit cell, further confirming the structural integrity of these monolayers.

Notably, a relatively flat optical phonon branch appears between 400–600 cm^{-1} in Ge-containing systems ($MgGe_2N_4$ and $MgGeSiN_4$) but is absent in $MgSi_2N_4$. This can be attributed to the heavier atomic mass of Ge, which results in localized vibrational modes with reduced phonon group velocities in that frequency range. Although Ge–N bonds may be comparable to Si–N bonds, the mass effect dominates the phonon dispersion behavior, leading to flatter optical modes. A similar trend has been reported in materials such as group 2H-MX_2 (M = Nb, Ta and X = S, Se), where the presence of heavier Ta atoms leads to flatter optical branches due to stronger localization of vibrations, reduced charge transfer, and lower bonding dispersion.[38]

To further assess the thermal stability of the proposed monolayers, we performed *ab initio* molecular dynamics (AIMD) simulations at room temperature (300 K). The energy fluctuations over time and the final equilibrium configurations after heating are depicted in Fig. 3(d–f). As evident, no signs of bond breaking or significant structural distortions are observed throughout the 5 ps simulation period, indicating that the monolayer frameworks remain structurally intact and closely resemble their initial relaxed geometries. These findings confirm that all three monolayers exhibit excellent thermal robustness under ambient conditions.

3.2 Electronic structure and magnetic properties

To investigate the electronic properties of the 2D MgZ_2N_4 (Z = Si, Ge) and Janus $MgGeSiN_4$ monolayers, we first performed spin-polarized band structure (BS) and orbital-projected density of states (PDOS) calculations using the PBE functional.[23] It is well-known that the PBE method tends to underestimate the band gaps of semiconductors and insulators. To overcome this limitation and provide more accurate predictions suitable for experimental validation, we employed the HSE06 hybrid functional.[25] The band structures obtained using both PBE and HSE06 are presented in Fig. 4 and 5, respectively, while the corresponding PDOS plots obtained with the PBE functional are shown in Fig. S3. The estimated band gap values for both spin channels, as computed using the PBE and HSE06 methods, are summarized in Table 2.

According to the PBE results, the $MgGe_2N_4$ monolayer exhibits an AFM metallic character, as indicated by the symmetric spin-up and spin-down states. The Mg-s, Ge-p, and N-p orbitals all contribute at the Fermi level (E_F), with the N-p orbitals providing the most significant contribution. In contrast, $MgSi_2N_4$ is found to be an intrinsic 100% spin-polarized half-metal, exhibiting an indirect band gap of 3.37 eV between the valence band maximum (VBM) at the Γ-point and the conduction band minimum (CBM) at the M-point of the Brillouin zone (BZ). In this system, the spin-up channel is semiconducting, with VBM arising mainly from N-p states and deeper bands (6–3 eV) further contributed by Mg-s and Si-p states. Meanwhile, the spin-down channel is metallic due to significant contributions from N-p orbitals.

Interestingly, the Janus $MgGeSiN_4$ monolayer exhibits intermediate characteristics between $MgGe_2N_4$ and $MgSi_2N_4$. It retains the metallic behavior of $MgGe_2N_4$, but features antiparallel spin alignment with spontaneous net magnetization, indicative of a ferrimagnetic (FiM) metallic state. In this case, the VB is mainly composed of hybridized Mg-s, Ge-p, Si-p, and N-p orbitals, with N-p orbitals dominating both the VBM and CBM.

When the HSE06 functional is applied, the calculated band gap of $MgSi_2N_4$ significantly increases due to an upward shift of the CBM, while its FM nature remains unchanged. The obtained HSE06 band gap for the majority-spin channel is 7.85 eV, classifying the material as an ultra-wide band gap (UWBG) ferromagnetic insulator. Notably, the CBM shows a pronounced dispersion, suggesting a low effective mass for electrons and potentially high electron mobility. In contrast, the flat dispersion near the VBM implies a high hole effective mass and low hole mobility. For the $MgGe_2N_4$ monolayer, the obtained HSE06 band structure shows FiM ordering, while the metallic nature is preserved. Janus $MgGeSiN_4$ also maintains its metallic FiM character under the HSE06 functional, in agreement with the PBE results.

Previous theoretical studies on MZ_2N_4-type monolayers, such as VSi_2N_4, $NbSi_2N_4$, $NbGe_2N_4$, $TaGe_2N_4$, and YSi_2N_4,[11,12] have reported semiconducting ferromagnetism, while YSi_2N_4 has been identified as a metallic ferromagnet.[12] Additionally, $ScSi_2N_4$ was predicted to be a half-metal,[13] and $HfCr_2N_4$ exhibits strain-tunable antiferromagnetic ground states.[14] However, to our knowledge, none of the previously studied MZ_2N_4 materials have been reported to exhibit a ground state of FiM, which marks our systems as a novel addition to this family.

The magnetic behavior of $MgGe_2N_4$, $MgSi_2N_4$, and Janus $MgGeSiN_4$ monolayers was systematically evaluated through both total and atom-projected magnetic moment analyzes. As summarized in Tables 2 and S1, the $MgGe_2N_4$ monolayer exhibits a negligible yet non-zero net magnetic moment of $-0.01\mu_B$, primarily arising from weak spin polarization in N atoms. This behavior is consistent with the subtle spin asymmetry near the E_F in the spin-resolved electronic structure, indicative of a weak FiM metallic character rather than a strictly AFM ground state.

In contrast, replacing Ge with Si in $MgSi_2N_4$ induces a significant transformation in the magnetic character. The $MgSi_2N_4$ monolayer exhibits a robust FM ground state with a total magnetic moment of $5.62\mu_B$, almost entirely contributed by N atoms ($5.66\mu_B$), while Mg and Si atoms remain magnetically inactive. According to Hund's rule, an isolated N atom is expected to exhibit a magnetic moment of $\sim 3.87\mu_B$ due to three unpaired 2p electrons. In the $MgSi_2N_4$ lattice, Bader charge analysis reveals significant electron transfer from Mg ($+1.60e^-$) and Si ($+2.53e^-$) to the surrounding N atoms (-2.21 to $-2.39e^-$), resulting in pronounced charge accumulation at N sites. This is further supported by previously discussed ELF values (0.65–0.75), suggesting partial electron localization and incomplete spin pairing in N. Consequently, the emergence of spin-

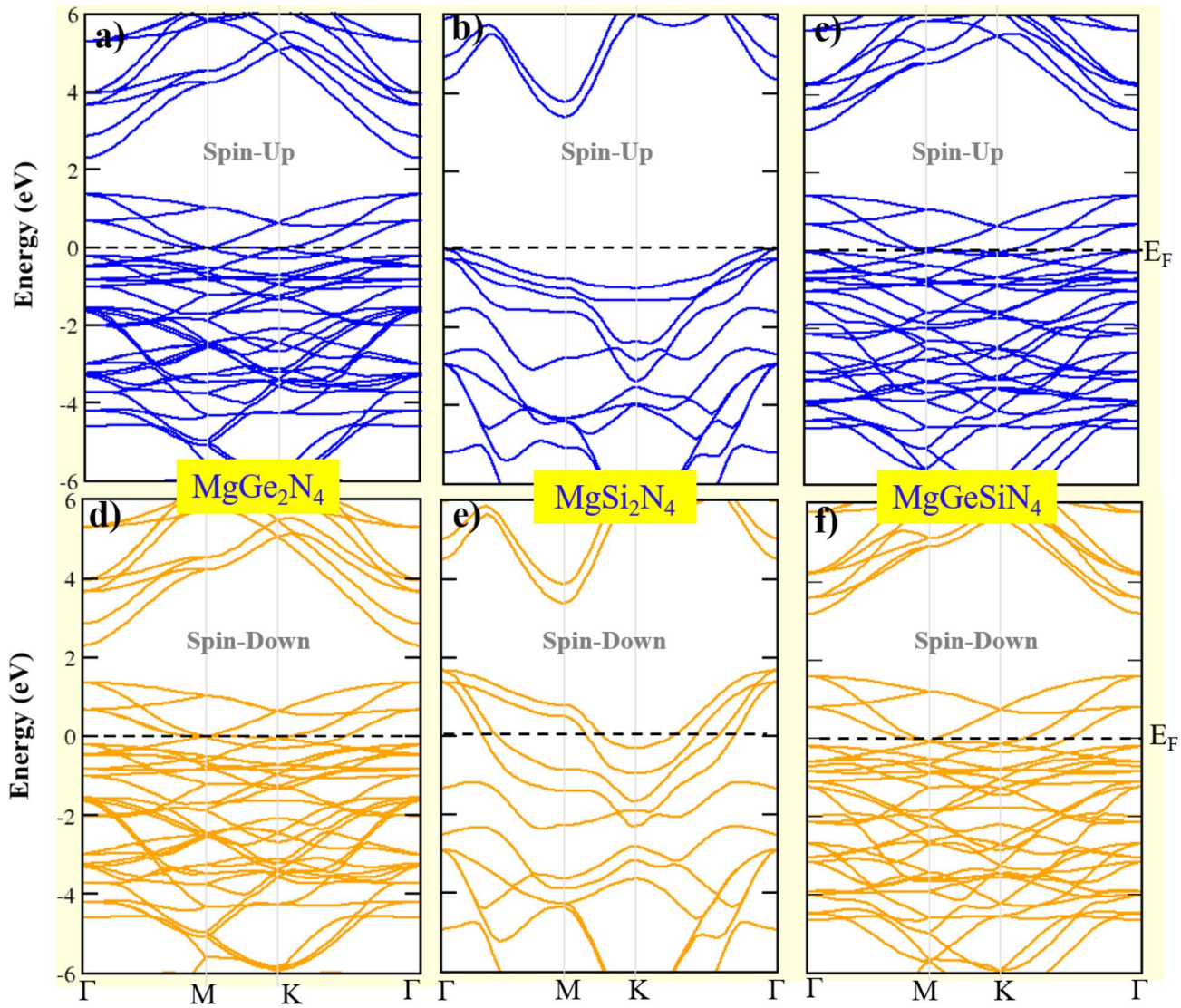

Fig. 4 (a–f) Spin-polarized electronic band structures of MgZ_2N_4 (Z = Ge, Si) and Janus $MgGeSiN_4$ monolayers calculated using the PBE functional. The Fermi level is indicated by a dashed black line.

polarized 2p states leads to a sizable net moment, primarily of N origin.

Interestingly, the Janus $MgGeSiN_4$ monolayer exhibits a net moment of $-0.22\mu_B$, stemming from unequal and oppositely aligned spin contributions from N ($-0.24\mu_B$), Ge ($-0.02\mu_B$), and Si ($+0.04\mu_B$). This spin imbalance confirms a FiM metallic ground state in the Janus configuration, attributable to the intrinsic asymmetry in its composition and charge distribution.

The observation that N atoms dominate the total magnetism across all three systems merits further attention. In the MA_2Z_4-type lattice, N atoms occupy both the central and outer layers and form covalent bonds with the electropositive Mg and group-IV Z elements (Ge, Si). Owing to their higher electronegativity, N atoms attract significant charge, leading to a strong p–s and p–p orbital hybridization. This interaction results in spin-dependent charge redistribution and partial occupation of N 2p orbitals, breaking spin degeneracy and giving rise to net magnetic moments.

Moreover, in the Janus configuration, symmetry breaking enhances this spin asymmetry, as the bonding environments above and below the N layers become inequivalent, leading to localized spin imbalances. The HSE06 further reveals this subtle effect more clearly than PBE, as it better captures the localized nature of N's 2p electrons. This mechanism of p-orbital-driven magnetism, in the absence of transition-metal d-states, highlights the pivotal role of nitrogen in mediating magnetism within MgZ_2N_4-based monolayers and underscores the unique nature of p-electron magnetism in low-dimensional, transition-metal-free systems.

Magnetic anisotropy energy (MAE) plays a pivotal role in determining the thermal stability of long-range magnetic ordering and the feasibility of high-density information storage in 2D magnetic materials.[39] The MAE defines the easy and hard axes of magnetization which is evaluated as the energy difference between in-plane and out-of-plane magnetization orientations, *i.e.*, $MAE = E_{\parallel} - E_{\perp}$, where a negative value indicates an in-plane

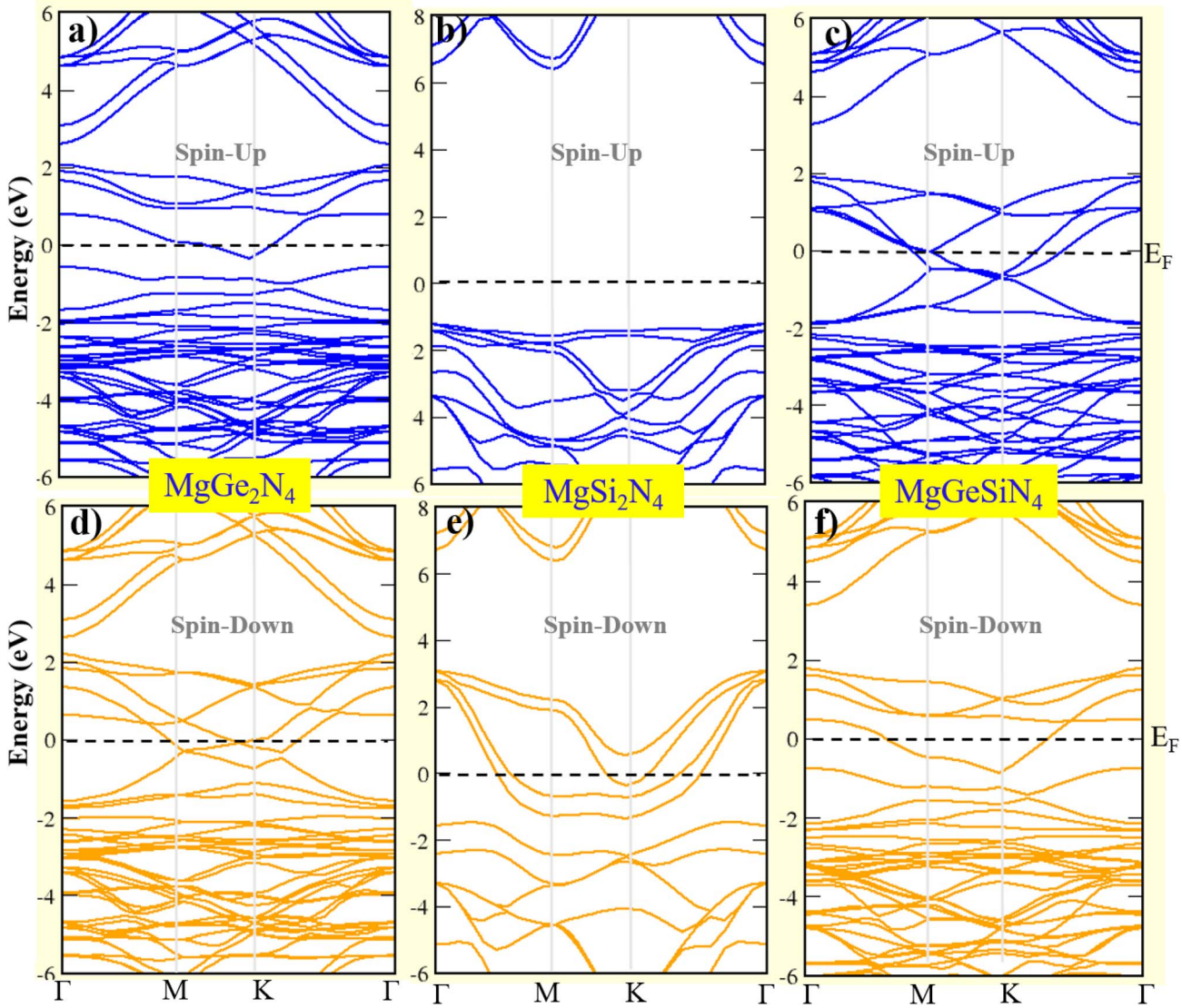

Fig. 5 (a–f) Spin-polarized electronic band structures of MgZ_2N_4 (Z = Ge, Si) and Janus $MgGeSiN_4$ monolayers calculated using the HSE functional. The Fermi level is indicated by a dashed black line.

Table 2 Electronic and magnetic properties of selected 2D materials: band gap using PBE and HSE for spin-up and spin-down states (eV), total magnetic moment (M_{tot}), magnetic anisotropy energy (MAE), energy difference between AFM and FM states (ΔE_{AFM-FM}), and Berezinskii–Kosterlitz–Thouless temperature (T_{BKT}) of MgZ_2N_4 (Z = Ge, Si) and Janus $MgGeSiN_4$ monolayers

Material	$E_g^{\uparrow}$ (PBE)	$E_g^{\downarrow}$ (PBE)	$E_g^{\uparrow}$ (HSE)	$E_g^{\downarrow}$ (HSE)	M_{tot} (μ_B)	MAE (μeV)	ΔE_{AFM-FM} (eV)	T_{BKT} (K)
$MgGe_2N_4$	Metal	Metal	Metal	Metal	−0.01	−50	−0.015	19
$MgSi_2N_4$	3.37	Metal	7.85	Metal	5.62	−30	+0.003	4
$MgGeSiN_4$	Metal	Metal	Metal	Metal	−0.22	−50	−0.012	16

(easy-axis) orientation and a positive value corresponds to an out-of-plane (easy-axis) orientation. The physical origin of MAE lies in direction-dependent magnetic interactions, governed primarily by spin–orbit coupling (SOC) rather than classical dipole–dipole interactions.[40] To quantify this, we performed noncollinear spin calculations including SOC to compute the total energies along four in-plane directions ([100], [010], [110], [111]) and one out-of-plane direction ([001]). The relative energies (in μeV per unit cell) with respect to the [001] direction are presented in Table S1, while the corresponding MAE values are summarized in Table 2. All three monolayers exhibit negative MAE values, confirming a preference for in-plane magnetization. Notably, $MgSi_2N_4$ shows the smallest MAE magnitude, indicating weaker anisotropy compared to $MgGe_2N_4$ and Janus $MgGeSiN_4$, both of which exhibit the same MAE and could be modulated more easily by external perturbations such as strain or defects.

Due to their small MAE values, these systems can be categorized as weak 2D-XY magnets, similar to the $CrCl_3$ monolayer.[41] However, their MAE magnitudes remain higher than those of other reported 2D magnets, such as $VSiGeN_4$ (−20 μeV), $VSiSnN_4$ (−10 μeV), and VSi_2P_4 (−4 μeV).[16,42]

In 2D magnetic systems with easy-plane anisotropy, magnetic ordering does not follow the conventional route of spontaneous symmetry breaking seen in three-dimensional (3D) materials. Instead, these systems may exhibit a BKT transition, a topological phase transition characterized by the unbinding of vortex–antivortex pairs at a critical temperature. Below the BKT transition temperature, the systems develop quasi-long-range order, where spin–spin correlations decay algebraically rather than exponentially, and the correlation length diverges as the transition is approached from above[43]

According to the Mermin–Wagner theorem, true long-range magnetic order is forbidden at finite temperatures in two-dimensional systems with continuous symmetry and short-range interactions, such as the isotropic Heisenberg model.[44] However, the inclusion of magnetic anisotropy alters this behavior. Easy-axis anisotropy (Ising-like) can support true long-range order, while easy-plane anisotropy (XY-like) enables the BKT transition.[43,45] Even weak anisotropies or spin–orbit interactions can open an energy gap in the spin-wave spectrum, stabilizing magnetism to some extent at finite temperatures.[46]

The studied monolayers $MgGe_2N_4$, $MgSi_2N_4$, and $MgGeSiN_4$ exhibit in-plane magnetic anisotropy and magnetic behavior that is consistent with the XY model, indicating the possibility of BKT-type ordering as observed in other two-dimensional magnets such as monolayer MnS[47] and B_6P_6X (X = Cl, Te),[8] rather than undergoing a conventional Curie or Néel transition. Indeed, the analysis of these monolayers' magnetic properties proves that the transition in magnetic ordering from antiferro- to ferro- to ferri-magnetic states explicitly shows that they are of the BKT-type. The transition temperature for such a BKT phase can be approximated using the XY model as:

$$T_C = 0.89(E_{AFM} - E_{FM})/8k_B \quad (4)$$

Here, $E_{AFM} - E_{FM}$ denotes the energy difference between the AFM and FM states (as reported in Table 2), and k_B is the Boltzmann constant. The computed T_{BKT} values for the $MgGe2N_4$, $MgSi_2N_4$, and Janus $MgGeSiN_4$ monolayers are approximately 19 K, 4 K, and 16 K, respectively, as listed in Table 2. These low T_{BKT} values reflect relatively weak exchange interactions, as indicated by the small energy differences—on the order of a few meV—between the magnetic configurations. This aligns with theoretical expectations. Notably, although $MgSi_2N_4$ exhibits a large M_{tot} and HMF behavior, its low T_{BKT} suggests that thermal fluctuations can readily disrupt its long-range ferromagnetic order. This apparent discrepancy likely arises from weak interatomic exchange interactions, possibly due to the spatial localization of magnetic moments on the nitrogen sites.

The predicted T_{BKT} values for the $MgGeN_4$ and Janus $MgGeSiN_4$ monolayers exceed those of previously reported materials such as B_6P_6Cl (∼5 K)[8] and $CrCl_3$ (∼13 K).[41] In contrast, the T_{BKT} of $MgSiN_4$ is comparable to that of ultrathin NbN films (∼4 K),[48] and notably higher than that of the $AuSn_4$ single crystal (∼2.4 K).

4 Conclusion

In summary, we have proposed a new family of 2D light-element-based materials—pristine MgZ_2N_4 (Z = Si, Ge) and their Janus derivative $MgGeSiN_4$—and conducted a comprehensive first-principles investigation of their structural, electronic, and magnetic properties. Cohesive and formation energy calculations, phonon dispersion analysis, and *ab initio* molecular dynamics simulations confirm that all three monolayers are energetically favorable and thermodynamically, dynamically and thermally stable at room temperature. Among them, $MgSi_2N_4$ emerges as a half-metallic ferromagnet with 100% spin polarization, featuring an ultra-wide band gap in the spin-up channel and metallic behavior in the spin-down channel. In contrast, both $MgGe_2N_4$ and Janus $MgGeSiN_4$ exhibit metallic ferrimagnetic ground states, characterized by spin asymmetry near the Fermi level. These differences originate from variations in orbital hybridization, primarily involving N-2p orbitals interacting with Mg-s, Si-p, and Ge-p states, which collectively shape the spin-resolved electronic structures. Magnetically, $MgSi_2N_4$ displays a robust magnetic moment of $5.62\mu_B$ per unit cell, making it a compelling candidate for spintronics applications. In contrast, $MgGe_2N_4$ and $MgGeSiN_4$ possess significantly lower net magnetic moments due to antiparallel spin alignment—an attribute that can be advantageous in spin-sensitive devices. Importantly, all three monolayers exhibit a weak in-plane magnetic anisotropy, suggesting that their magnetic behavior is governed by the 2D XY model, which allows for BKT transitions rather than conventional long-range order. The estimated BKT transition temperatures—approximately 19 K for $MgGe_2N_4$, 4 K for $MgSi_2N_4$, and 16 K for $MgGeSiN_4$—reflect relatively weak exchange interactions, yet confirm the possibility of achieving quasi-long-range magnetic order at low temperatures. These results highlight not only the richness of magnetic phases—by presenting, for the first time, intrinsic FM, AFM, and FiM ordering within this monolayer family—but also their potential for integration into low-temperature spin-based technologies, where 2D magnetism and BKT physics play a crucial role.

Author contributions

Warda Elaggoune: sonceptualization, formal analysis, investigation, visualization, validation, writing – original draft. Yusuf Zuntu Abdullahi: conceptualization, formal analysis, investigation, methodology, software, supervision, validation, writing – review & editing. Sohail Ahmad: project administration, supervision, validation. Lim Thong Leng: project administration, supervision, validation.

Conflicts of interest

The authors declare that they have no known competing financial interests or personal relationships that could have appeared to influence the work reported in this paper.

Data availability

The data of this study are available from the corresponding author upon reasonable request.

The Supplementary information file contains: (i) magnetic configurations of pristine MgZ_2N_4 (Z = Ge, Si) and Janus $MgGeSiN_4$ monolayers; (ii) histograms comparing Young's modulus and Poisson's ratio with related compounds; (iii) spin-polarized total and projected density of states (TDOS/PDOS) from PBE calculations; and (iv) a summary table of magnetic moments, total energies of FM, AFM, and NM states, and magnetocrystalline anisotropy energies. See DOI: **https://doi.org/10.1039/d5ra03942h**.

Acknowledgements

The authors extend their appreciation to the Deanship of Research and Graduate Studies at King Khalid University for funding this work through Large Research Groups Project under grant number RGP2/614/46.

References

1 K. S. Novoselov, A. K. Geim, S. V. Morozov, D.-e. Jiang, Y. Zhang, S. V. Dubonos, I. V. Grigorieva and A. A. Firsov, *Science*, 2004, **306**, 666–669.
2 W. Elaggoune, *PhD thesis*, University of 8 May 1945 Guelma, Algeria, 2024.
3 K. L. Seyler, D. Zhong, D. R. Klein, S. Gao, X. Zhang, B. Huang, E. Navarro-Moratalla, L. Yang, D. H. Cobden, M. A. McGuire, *et al.*, *Nat. Phys.*, 2018, **14**, 277–281.
4 D. R. Klein, D. MacNeill, J. L. Lado, D. Soriano, E. Navarro-Moratalla, K. Watanabe, T. Taniguchi, S. Manni, P. Canfield, J. Fernández-Rossier, *et al.*, *Science*, 2018, **360**, 1218–1222.
5 Z. Chen, Y. Yang, T. Ying and J.-g. Guo, *Nano Lett.*, 2024, **24**, 993–1000.
6 Y.-L. Hong, Z. Liu, L. Wang, T. Zhou, W. Ma, C. Xu, S. Feng, L. Chen, M.-L. Chen, D.-M. Sun, *et al.*, *Science*, 2020, **369**, 670–674.
7 L. Wang, Y. Shi, M. Liu, A. Zhang, Y.-L. Hong, R. Li, Q. Gao, M. Chen, W. Ren, H.-M. Cheng, *et al.*, *Nat. Commun.*, 2021, **12**, 2361.
8 W. Elaggoune and Y. Z. Abdullahi, *J. Phys. Chem. Solids*, 2024, **194**, 112256.
9 S. Li, W. Wu, X. Feng, S. Guan, W. Feng, Y. Yao and S. A. Yang, *Phys. Rev. B*, 2020, **102**, 235435.
10 S.-D. Guo, W.-Q. Mu, Y.-T. Zhu and X.-Q. Chen, *Phys. Chem. Chem. Phys.*, 2020, **22**, 28359–28364.
11 L. Wang, Y. Shi, M. Liu, Y.-L. Hong, M.-X. Chen, R. Li, Q. Gao, W. Ren, H.-M. Cheng, Y. Li, *et al.*, *Nat. Commun.*, 2021, **12**(1), 2361.
12 Y. Ding and Y. Wang, *J. Phys. Chem. C*, 2021, **125**, 19580–19591.
13 Z. Zhao, X. Duan, X. Fang, X. Wang and W. Mi, *Appl. Surf. Sci.*, 2023, **611**, 155693.
14 D. Zhang, H. Ye, M. Su and J. Wang, *Phys. Rev. B*, 2024, **110**, 155403.
15 L. A. Freeman, J. E. Walley and R. J. Gilliard Jr, *Nat. Synth.*, 2022, **1**, 439–448.
16 D. Dey, A. Ray and L. Yu, *Phys. Rev. Mater.*, 2022, **6**, L061002.
17 X. Guo and S. Guo, *J. Semicond.*, 2021, **42**, 122002.
18 D. Dey, A. Ray and L. Yu, *APS March Meeting Abstracts*, 2023, p. N55-009.
19 G. Kresse and J. Hafner, *Phys. Rev. B: Condens. Matter Mater. Phys.*, 1993, **47**, 558.
20 G. Kresse and J. Hafner, *Phys. Rev. B: Condens. Matter Mater. Phys.*, 1994, **49**, 14251.
21 G. Kresse and J. Furthmüller, *Comput. Mater. Sci.*, 1996, **6**, 15–50.
22 G. Kresse and J. Furthmüller, *Phys. Rev. B: Condens. Matter Mater. Phys.*, 1996, **54**, 11169.
23 J. P. Perdew, K. Burke and M. Ernzerhof, *Phys. Rev. Lett.*, 1996, **77**, 3865.
24 P. E. Blöchl, *Phys. Rev. B: Condens. Matter Mater. Phys.*, 1994, **50**, 17953.
25 J. Heyd, G. E. Scuseria and M. Ernzerhof, *J. Chem. Phys.*, 2003, **118**, 8207–8215.
26 S. Grimme, J. Antony, S. Ehrlich and H. Krieg, *J. Chem. Phys.*, 2010, **132**, 15.
27 R. F. Bader, *Acc. Chem. Res.*, 1985, **18**, 9–15.
28 X. Gonze and C. Lee, *Phys. Rev. B: Condens. Matter Mater. Phys.*, 1997, **55**, 10355.
29 V. Wang, N. Xu, J.-C. Liu, G. Tang and W.-T. Geng, *Comput. Phys. Commun.*, 2021, **267**, 108033.
30 M.-Y. Liu and Y. He and X. Li and K. Xiong, *Strain-Engineered Electronic, Valley, and Photocatalytic Properties in Janus Wsigez4 (Z = N, P, as) Monolayers*, Available at SSRN: **https://ssrn.com/abstract=4253465** or DOI: **10.2139/ssrn.4253465**.
31 M. J. Varjovi, E. Durgun, G. Pacchioni and S. Tosoni, *Phys. Rev. Mater.*, 2024, **8**, 074004.
32 R. Mao and Z. Li, *Phys. Lett. A*, 2025, **534**, 130260.
33 I. Waller, *Acta Crystallogr.*, 1956, **9**(10), 837–838.
34 W. Elaggoune, A. Meddour, C. Bourouis, M. H. Gous and Z. Bordjiba, *Solid State Commun.*, 2023, **361**, 115060.
35 W. Elaggoune, A. Meddour and C. Bourouis, *Mater. Sci. Semicond. Process.*, 2023, **165**, 107684.
36 W. Elaggoune, F. Ersan and A. Meddour, *RSC Adv.*, 2024, **14**, 20668–20682.
37 S. Ahmad, H. Din, C. Q. Nguyen, S.-T. Nguyen and C. Nguyen, *Dalton Trans.*, 2024, **53**, 3785–3796.
38 D. Lin, S. Li, J. Wen, H. Berger, L. Forró, H. Zhou, S. Jia, T. Taniguchi, K. Watanabe, X. Xi, *et al.*, *Nat. Commun.*, 2020, **11**, 2406.
39 H. Huang, Y. Zhao, Z. Zhang, L. Wang, Y. Wu, C. Liu, J. Zhao, G. Qiao, J. Zhang, X. Zheng, *et al.*, *APL Mater.*, 2024, **12**, year.
40 R. Singla, T. A. Hackett, S. Kumar, J. Sharma and M. K. Kashyap, *Nanoscale Adv.*, 2020, **2**, 5890–5896.
41 X. Cai, T. Song, N. P. Wilson, G. Clark, M. He, X. Zhang, T. Taniguchi, K. Watanabe, W. Yao, D. Xiao, *et al.*, *Nano Lett.*, 2019, **19**, 3993–3998.
42 G. Hussain, A. Fakhredine, R. Islam, R. M. Sattigeri, C. Autieri and G. Cuono, *Materials*, 2023, **16**, 1649.

43 J. M. Kosterlitz and D. J. Thouless, *J. Phys. C: Solid State Phys.*, 1973, **6**, 1181.
44 N. D. Mermin and H. Wagner, *Phys. Rev. Lett.*, 1966, **17**, 1133.
45 C. N. Yang, *Phys. Rev.*, 1952, **85**, 808.
46 J. Stöhr and H. C. Siegmann, *Solid State Sci.*, 2006, **5**, 236.
47 Y. Z. Abdullahi, *Gazi Univ. J. Sci.*, 2024, **1**, 1.
48 J. Yong, T. Lemberger, L. Benfatto, K. Ilin and M. Siegel, *Phys. Rev. B: Condens. Matter Mater. Phys.*, 2013, **87**, 184505.